

# THE HYDROGEN EPOCH OF REIONIZATION ARRAY DISH I: BEAM PATTERN MEASUREMENTS AND SCIENCE IMPLICATIONS

ABRAHAM R. NEBEN<sup>1</sup>, RICHARD F. BRADLEY<sup>2,3</sup>, JACQUELINE N. HEWITT<sup>1</sup>, DAVID R. DEBOER<sup>4</sup>, AARON PARSONS<sup>4</sup>, JAMES E. AGUIRRE<sup>6</sup>, AARON EWALL-WICE<sup>1</sup>, NIPANJANA PATRA<sup>4</sup>, NITHYANANDAN THYAGARAJAN<sup>5</sup>, ZAKI S. ALI<sup>4</sup>, JUDD BOWMAN<sup>5</sup>, CARINA CHENG<sup>4</sup>, ROGER DICKENSON<sup>3</sup>, PHILLIP DOOLITTLE<sup>3</sup>, DENNIS EGAN<sup>3</sup>, MIKE HEDRICK<sup>3</sup>, SAUL A. KOHN<sup>6</sup>, BENJAMIN R.B. SALIWANCHIK<sup>7</sup>, PATRICK SCHAFFNER<sup>3</sup>, JOHN SHELTON<sup>3</sup>, H.A. TAYLOR<sup>3</sup>, RUSTY TAYLOR<sup>3</sup>, BUTCH WIRT<sup>3</sup>, JEFF ZHENG<sup>1</sup>

<sup>1</sup>MIT Kavli Institute, Massachusetts Institute of Technology, Cambridge, MA, 02139 USA

<sup>2</sup>Dept. of Electrical and Computer Engineering, University of Virginia, Charlottesville, VA 22904

<sup>3</sup>National Radio Astronomy Obs., Charlottesville, VA

<sup>4</sup>Dept. of Astronomy, University of California, Berkeley, CA, USA

<sup>5</sup>Arizona State University, School of Earth and Space Exploration, Tempe, AZ 85287, USA

<sup>6</sup>Dept. of Physics and Astronomy, University of Pennsylvania, Philadelphia, PA and

<sup>7</sup>Astrophysics and Cosmology Research Unit, University of KwaZulu-Natal, Durban, South Africa

*Draft version February 4, 2016*

## ABSTRACT

The Hydrogen Epoch of Reionization Array (HERA) is a radio interferometer aiming to detect the power spectrum of 21 cm fluctuations from neutral hydrogen from the Epoch of Reionization. Drawing on lessons from the Murchison Widefield Array (MWA) and the Precision Array for Probing the Epoch of Reionization (PAPER), HERA is a hexagonal array of large (14 m diameter) dishes with suspended dipole feeds with element collecting area of 100 m<sup>2</sup>. Not only does the dish determine overall sensitivity, it determines the aggregate frequency structure of foregrounds in the interferometer. This is the first of a series of four papers characterizing the frequency and angular response of the with simulations and measurements. We focus in this paper on the angular response (i.e., power pattern), which sets the relative weighting between sky regions of high and low delay, and thus, apparent source frequency structure. We measure the angular response at 137 MHz using the ORBCOMM beam mapping system of Neben et al. (2015). We measure a collecting area of 93 m<sup>2</sup> in the optimal dish/feed configuration, implying HERA-331 should detect the EOR power spectrum with a signal-to-noise ratio of 19.3 using a foreground avoidance approach, and 74.3 using a foreground subtraction approach. Lastly we study the impact of these beam measurements on the distribution of foregrounds in Fourier space.

*Subject headings:* instrumentation: interferometers — techniques: interferometric — cosmology: observations — dark ages, reionization, first stars

## 1. INTRODUCTION

A new generation of low frequency radio telescopes is coming online with the goal of probing redshifted 21 cm emission from the Cosmic Dawn. These observations will complement indirect probes of the Dark Ages and Epoch of Reionization such as quasar sightlines and the CMB optical depth which leave the reionization history of the universe only loosely constrained. (See Furlanetto et al. (2006); Morales & Wyithe (2010); Pritchard & Loeb (2012); Loeb & Furlanetto (2013); Zaroubi (2013) for reviews) Sensitivity and foreground removal are the main challenges in 21 cm observations, as the expected cosmological signal is 4–5 orders of magnitude fainter in brightness temperature than Galactic and extragalactic foregrounds. Radio interferometers such as the Murchison Widefield Array (MWA) (Tingay et al. 2013; Bowman et al. 2013), the Precision Array for Probing the Epoch of Reionization (PAPER) (Ali et al. 2015b), the Giant Meterwave Radio Telescope (GMRT) (Paciga et al. 2011), and the Low Frequency Array (LOFAR) (van Haarlem et al. 2013) are seeking a first detection of cosmological 21 cm emission in power spectrum measurements, where the smooth frequency evolution of the foreground emission separates from the spectrally rough cosmological signal whose frequency dimension probes a line of sight through the inhomogeneous reionizing universe.

The Hydrogen Epoch of Reionization Array (HERA)

(Pober et al. 2014, deBoer et al. (in prep)) is drawing on lessons learned by the MWA and PAPER to reach the calibration and foreground isolation accuracy required to make a significant detection and characterization of the cosmological signal. HERA uses 14 m diameter parabolic dishes arranged in a compact, hexagonal array to achieve coherent integration of the very low surface brightness 21 cm signal. Redundant baselines also permit redundant calibration techniques which solve for the relative calibration between all antennas (Liu et al. 2010; Zheng et al. 2014). A central lesson from first generation instruments is that it is essential to characterize the instrument response to foreground emission lest instrument frequency dependence smear foreground power into cosmological signal modes.

In an ideal achromatic instrument the foreground emission would be confined to the lowest few line of sight Fourier modes (e.g., Morales et al. 2006), however the interferometer’s frequency-dependent point spread function smears foreground power into a “wedge” shaped region in  $(k_{\perp}, k_{\parallel})$  Fourier space (Datta et al. 2010; Dillon et al. 2014; Pober et al. 2013; Morales et al. 2012; Vedantham et al. 2012; Thyagarajan et al. 2013; Trott et al. 2012; Liu et al. 2014a,b; Parsons et al. 2012b). This effect is straightforward to understand for a single baseline which measures the sky intensity weighted by the complex sky fringe  $e^{i\vec{k}\cdot\vec{b}}$ , where  $\vec{k}(\nu)$  is the wave vector of

incident radiation pointing along its direction of travel,  $\vec{b}$  is the baseline vector in meters, and  $\nu$  is the observation frequency. Thus sources at different positions relative to the baseline vector manifest different frequency structure despite their intrinsically smooth spectra, but are geometrically limited by the baseline length to a maximum frequency dependence of  $e^{2\pi i \nu \tau_g}$ , where  $\tau_g = \vec{b} \cdot \hat{k} / c$  is the delay in radiation arrival time between the two antennas in the baseline. This limits the foreground contamination to a wedge shaped region in Fourier space with  $k_{\parallel} < a k_{\perp}$ , where  $k_{\perp}$  and  $k_{\parallel}$  represent spatial modes perpendicular and parallel to the line of sight, and  $a$  is a constant depending on the observational frequency and cosmology. The complement of the wedge is known as the “EOR window”.

It is convenient to phrase this description in terms of the delay in radiation arrival at the baseline’s two antennas,  $\tau$ , where  $\tau_{\max} = b/c$ . Sources at low delay have little frequency structure, while those near  $\tau = \tau_{\max}$  acquire the maximum frequency structure given the baseline length. The high delay regions of the sky lie near the horizon while low delay regions lie closer to zenith and also perpendicular to the baseline vector.

So because sources acquire frequency dependence based on their position on the sky, and the primary beam weights different regions of the sky differently, we see that the primary beam (i.e., the antenna angular response) strongly affects the aggregate frequency dependence of the foregrounds. Thyagarajan et al. (2015a) simulate the foreground contamination seen with a dipole beam, a phased array, and a Airy pattern, and find that the latter suffers the least foreground leakage into  $k_{\parallel} > 0$  modes due to its narrow main lobe and minimal sidelobe levels. To be sure, all are subject to the same geometric limits on foreground frequency- dependence which limit foreground bounding foreground emission within the wedge, but the emission from high delay is better suppressed using the Airy pattern leaving much of the wedge effectively empty.

For foreground avoidance-based power spectrum estimation, so long as foreground emission is perfectly contained in the wedge it is irrelevant how much or little of it there is, but real world effects smear power beyond the geometrical edge of the wedge into the EOR window. Finite bandwidth, imperfect bandpass calibration, and faraday rotation (Jelić et al. 2010; Moore et al. 2013; Bernardi et al. 2013; Moore et al. 2013; Moore et al. 2015; Asad et al. 2015) of polarized sources can all imprint slight frequency structure on otherwise spectrally smooth sources, and those appearing closest to the edge of the wedge are most at risk of leaking into the EOR window. In fact, Thyagarajan et al. (2015a); Thyagarajan et al. (2015b) observe in simulations and then in data that while naively we might expect minimal emission at the very edge of the wedge because typical near-horizon beam responses are so small, two effects can cause a relative brightening of emission at those maximal delays, creating a characteristic “pitchfork” shape. This horizon brightening is caused by the large solid angle subtended by the near-horizon regions of the sky, as well as the apparent shortening of baselines when viewed nearly on axis at these elevations. This second effect makes intermediate length baselines of tens to hundreds of meters

sensitive to the very bright diffuse emission they would not see from near zenith. Together, these effects can overcome the decline in beam sensitivity near the horizon. All these considerations highlight the antenna beam as a critical design parameter for 21 cm observatories.

This is the first in a series of four papers detailing the HERA element. In this work we study the angular response of the dish and its implications for power spectrum measurements. The three companion papers present reflectometry measurements (Patra et al., submitted) and simulations (Ewall-Wice et al., submitted) of the dish frequency response, as well as detailed foreground simulations for HERA (Thyagarajan et al., submitted). A general description to the design of the HERA experiment is given by DeBoer et al. (in prep). In essence, we require a large collecting area for sensitivity and minimal sidelobes and horizon response without incurring the large cost per collecting area of very large dishes. A dish is preferred to a large phased array as it has a less complex beam pattern and reduced potential for antenna-to-antenna variation (Neben et al, submitted). The 331 dishes are positioned in a compact, hexagonal array permitting redundant baseline calibration and coherent integration in  $\vec{k}$  space (Zheng et al. 2014; Parsons et al. 2012a).

In this paper we first characterize the angular response of a prototype HERA dish at the National Radio Astronomy Observatory–Green Bank. We use the beam mapping system of Neben et al. (2015) to measure the 137 MHz beam pattern using the ORBCOMM satellite constellation. We obtain beam measurements out to zenith angles of  $\sim 60^\circ$  where the beam response is -35 dB relative to zenith, and compare with different numerical electromagnetic models. We characterize the dish beam at various feed heights to map out the focus and study beam errors due to feed misalignment. We compute the collecting areas and implied EOR power spectrum sensitivities of our measured beams. After verifying our models, we consider the science implications of these beam patterns by foreground delay spectra at different baseline lengths and observing conditions to study when the horizon brightening effect is strongest, and thus, when foreground are most at risk of leaking into the EOR window.

We discuss the electromagnetic design and modeling of the dish in Section 2. We present the experimental setup of the beam mapping experiments and discuss their systematics, then review the ORBCOMM beam measurement system in Section 3. We present our power pattern measurements in Section 4, and study the science implications of these beam measurements for foreground power spectra in Section 5, then conclude with discussion in Section 6.

## 2. DISH DESIGN AND MODELING

### 2.1. Design of the HERA Dish

The HERA element (Fig. 1) is a 14 m diameter faceted parabolic dish ( $f\# = 0.32$ ) with a dual-polarized dipole feed suspended at prime focus. The dish surface is formed by wire mesh sheets (i.e., facets) mounted on PVC tubes which run from the lip of the dish to the hub at the vertex. The feed consists of a dual linear polarization PAPER sleeved dipole mounted 17” below

a 78" diameter wire mesh back plane surrounded by a 30" deep cylinder, suspended from cables attached to each the three telephone poles around the dish. The dipole "sleeves" are circular disks just above and below the dipole designed to broaden its frequency response. The cylinder is offset 0.5" from the back plane, and is designed to make the beams for both linear polarizations more similar, and also to taper the dipole beam towards the edge of the dish to mitigate dish-dish coupling. Fig. 2 shows the feed as deployed on the ground for early testing. The nominal dish focus is  $f = (f\#)D = 4.48$  m, though our numerical electromagnetic models suggest the actual focus is slightly higher due to the feed geometry. In this work we study the dish beam pattern at feed heights of 4.5 m, 5.0 m, and 5.3 m, measured from dish surface to feed plane, the last height being the maximum height we can achieve with the feed suspension system installed on the dish. These height measurements are uncertain at the  $\pm 5\%$  level in this study. For more details on the dish design and construction see DeBoer et al. (in prep). Feed/dish optimization studies are ongoing and the values of these parameters may change in the full HERA array.

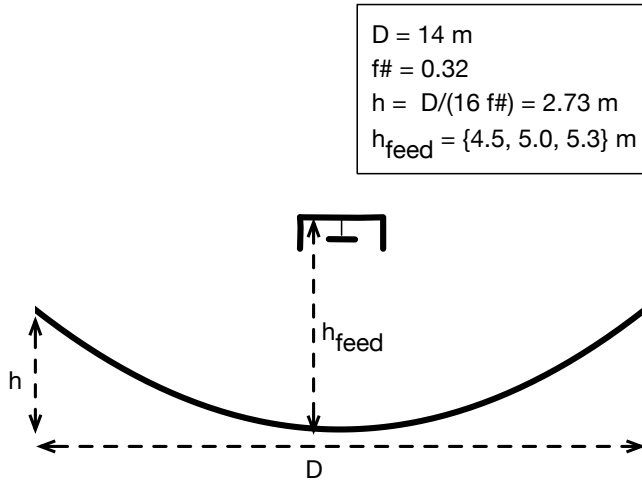


FIG. 1.— Diagram showing the dimensions and layout of the HERA dish and suspended feed.

As the HERA element is larger than the MWA or PAPER antenna elements, one might worry about the smaller field of view and thus smaller number of measured Fourier modes perpendicular to the line of sight. However, this is a small effect for 21 cm power spectrum analyses as our leverage on  $k$  modes comes primarily from modes along the line of sight (in the frequency dimension). Further, HERA's smaller field of view is actually desirable in that it drastically reduces the magnitude of emission at the edge of the wedge compared to a simple dipole element (Thyagarajan et al. 2015a). A second potential drawback is frequency structure introduced by time domain reflections between the dish and feed detailed by Ewall-Wice et al. (submitted) with simulations and Patra et al. (in prep) with zenith reflectometry measurements. These works demonstrate, though, that the slight frequency structure of the dish is sufficiently small to not interfere with EOR science.

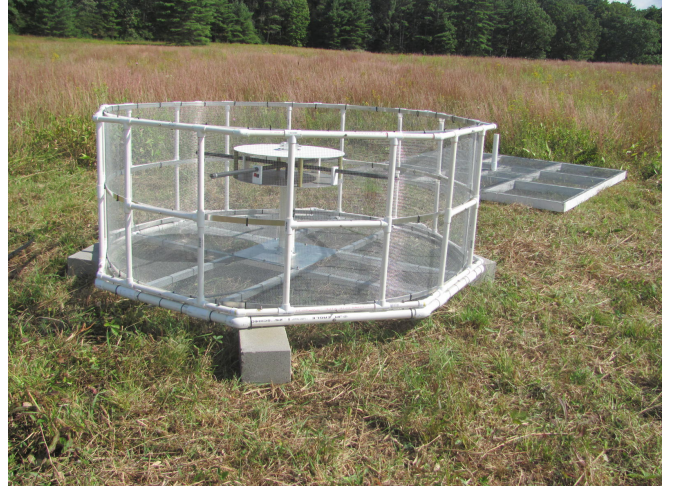


FIG. 2.— Prototype HERA feed set up outside the dish for preliminary characterization. This feed revision consists of a dual-polarized sleeved dipole offset 17" from a 78" diameter back plane, surrounded by a 30" deep cylindrical skirt.

## 2.2. Dish Modeling

We numerically model the HERA dish in both ANSYS HFSS<sup>1</sup> and in CST Microwave Studio<sup>2</sup>, making slightly different assumptions, in order to study the dependence of the beam pattern on modeling inaccuracies and material uncertainties. In particular, the near horizon beam response, which sets the level of horizon brightening in the delay spectrum, is quite sensitive to modeling assumptions. Modeling also probes the best focus of the dish-feed system.

The HFSS model assumes a solid 14 m parabolic dish ( $f\# = 0.32$ ) with a 1 m hole at the vertex. In reality a 1 m diameter circle at the vertex is filled with concrete and supports the PVC pipes which suspend the mesh panels, but we effectively assume here it is perfectly absorbant. The feed is modeled as sleeved dipole with a solid metal back plane and cylinder with the dimensions given above. Copper is used for the dipole itself, and aluminum for all reflecting surfaces. In the simulations, we excite one of the dipoles using a modal port and measure the total gain response in each direction to 137.5 MHz radiation.

The CST model again assumes a 14 m parabolic diameter solid aluminum paraboloid with  $f\# = 0.32$  but neglects the 1 m hole at the vertex, effectively assuming the concrete and earth ground behind it are perfectly reflective. The actual material properties are somewhere between these two models. The feed model has the same dimensions and properties as in the HFSS model. These simulations are done by exciting one of the dipoles with band-limited noise (100–200 MHz), then measuring the farfield radiation in each direction after the excitation pulse energy within the structure decays to below -80 dB.

The simulated HFSS and CST beams for the NS dipole are plotted in Fig. 3 (left and center panel) along with an Airy pattern for comparison. As expected, both model beams have slightly stronger sidelobes and wider main lobes than the ideal Airy pattern. The dipole sleeve (cir-

<sup>1</sup> <http://www.ansys.com/Products/Electronics/ANSYS-HFSS>

<sup>2</sup> <https://www.cst.com/Products/CSTMWS>

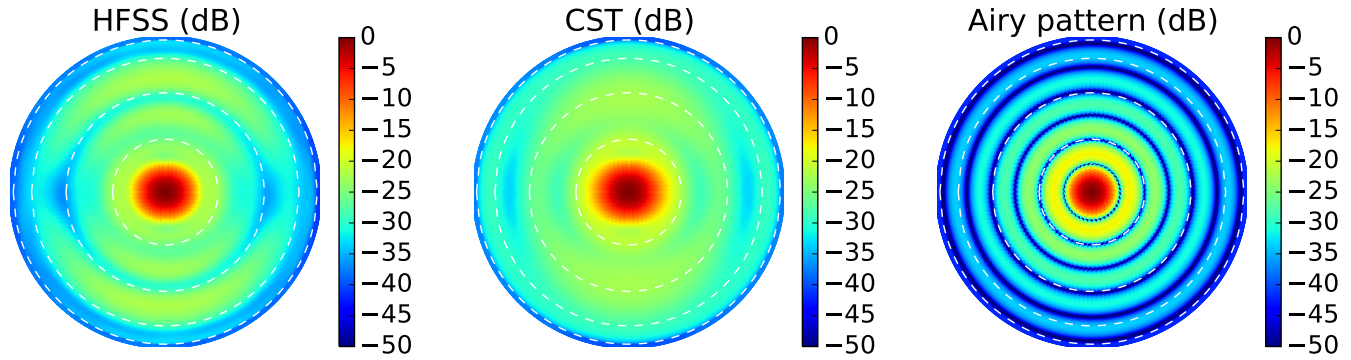


FIG. 3.— Simulated dish power patterns (NS polarization) at 137 MHz (see Sec. 2.2) with  $h_{\text{feed}} = 5$  m using HFSS (left) and CST (middle) are shown beside an ideal Airy pattern for a 14 m diameter dish for comparison.

cular pieces in Fig. 2) and skirt result in a feed beam which is slightly elongated in the E plane and slightly compressed in the H plane, opposite to the behavior of a simple dipole. This wider dish illumination in the NS direction by the NS feed dipole results in a narrower dish beam in the NS direction. Similarly, the EW dish beam is narrower in the EW direction. Lastly, we note that in both models, the best focus is found to be close to 5.23 m with this feed geometry, slightly larger than the nominal focus of 4.5 m, as expected.

### 3. EXPERIMENTAL SETUP

#### 3.1. ORBCOMM Beam Mapping System Review

We briefly review the beam mapping system detailed by Neben et al. (2015), then discuss the application of the system for HERA dish measurements. The system takes advantage of the 137 MHz communications satellites operated by ORBCOMM Inc. as bright point sources which, by virtue of their number ( $\sim 30$ ), short orbital periods ( $\sim 90$  minutes), and orbital precession, cover  $\sim 65\%$  of the visible sky in just a few days. The coverage from the Green Bank site is limited by the fact that the satellites' orbital inclinations are all less than  $45^\circ$ .

Unlike celestial source beam measurements, where the flux may be assumed constant over the timescale of the measurement, satellite fluxes can vary rapidly due to changing distance, orientation, and transmission power. To correct for this, we measure the satellite flux in each ground polarization (EW and NS) using a simple, well-modeled reference antenna. Comparison of this measured power with that observed in the Antenna-Under-Test (AUT) gives the AUT beam response in the direction of the satellite. An equivalent interpretation of the measurement is that the power ratio between the AUT and the reference antenna gives the relative beam response in the satellite direction, and multiplication by the reference antenna model yields the desired AUT response. As discussed in Neben et al. (2015), this procedure correctly measures the response of the AUT to unpolarized radiation despite the fact that satellite signals are generally polarized.

In detail, we measure the dual-polarization RMS power received by each antenna in 512 2 kHz channels across the 137–138 MHz band. Each band power is averaged over  $\sim 0.2$  sec. There are 0–3 satellites above the horizon at any given time transmitting on different  $\sim 15$  kHz wide sub-bands in 137–138 MHz. By observing at many

different frequencies, we probe the beam response in all these directions simultaneously. We compute the satellite positions using the orbital elements published by Celestrak<sup>3</sup> and the orbital integrator *predict*<sup>4</sup>. However, the satellite frequencies vary occasionally to avoid interference within the constellation. Zheng et al. (2014) use interferometric phases to identify and exclude times when multiple satellites are in view. As our data acquisition system makes only total power measurements, we instead use an ORBCOMM interface box (typically supplied to commercial users of the network) to connect to passing satellites and record their identifier and transmission frequency during each pass.

In this way, beam measurements are built up along satellite tracks over the course of several days of integration, yielding typically 200–300 satellite passes. Each pass is processed separately to identify and exclude times of low signal-to-background when the satellite is low in the sky or in the off state of a pulsing sequence. At those times, then satellite flux no longer dominates over that of the diffuse Galactic background, and a power measurement no longer probes the response in only the satellite direction. The beam measurements are then gridded in local Azimuth/Elevation coordinates in HEALPix (Górski et al. 2005) as discussed in Sec. 3.1.

#### 3.2. HERA–Green Bank: A three-element prototype array

A 3-element HERA engineering prototype is being constructed at the National Radio Astronomy Observatory–Green Bank. We performed the beam measurements presented in this work on the first of these dishes to be constructed, future work will characterize its beam in the presence of the other two dishes once they are constructed. The prototype array is situated in Galford Meadow, approximately 1 km southwest of the Green Bank Telescope. Note that unlike the full HERA site in the Karoo Desert Radio Astronomy Reserve in South Africa, the Green Bank site has trees and foothills, as well as moist ground. Our beam measurements are sensitive to these effects in addition to the construction imperfections of real world dishes.

We use a simple dual-polarization dipole as our reference antenna. The dipole is constructed out of copper tubing covered by PVC for protection, mounted above

<sup>3</sup> <http://www.celestrak.com/NORAD/elements/orbcomm.txt>

<sup>4</sup> <http://www.qsl.net/kd2bd/predict.html>





FIG. 4.— The dish with its suspended feed is seen in the back, 50 m north of one of the reference antennas used in the null experiment to study systematics. The experiment is conducted in Galford Meadow at NRAO–Green Bank. See Neben et al. (2015) for details. During the dish measurements the dipole is positioned 100 m due south of the dish, though we experiment with other locations in order to characterize the environmental systematics of these measurements, as detailed in the next section. Figure 4 shows the dish with suspended feed 50 m north of one of the reference antennas.

### 3.3. Assessing Experimental Systematics

As in Neben et al. (2015), we assess systematics using a “null experiment” in which we use a second reference dipole as the antenna-under-test (AUT). Taking the ratio of its measured power pattern with the model beam pattern amounts to a ratio of the raw power responses received by the two antennas as a function of satellite direction. This probes the level of environmental systematics (i.e., reflections and varying ground properties) and antenna fabrication imperfections which affect each antenna differently. This is not a probe of modeling imperfections common to both antennas, but we expect such errors to be subdominant as the physical properties of the antenna are easier to characterize, and thus simulate, than misalignments and local environmental effects.

As we are not able to replace the HERA dish with a reference antenna, we run two null experiments with both reference dipoles deployed (1) 50 m apart on a NS line, 50 m south of the HERA dish; and (2) 100 m apart on a NS line, 100 m south of the HERA dish. Figure 5 shows the results from these experiments in the form of the ratio of the power responses of the two antennas. We collected roughly 100 satellite passes. Systematics at the few percent level are observed in within  $20^\circ$  of zenith, and at the 10–20% level farther out. The magnitude and angular distribution of these systematics changes modestly as the separation is changed, suggesting that the reference dipoles differ largely due to intrinsic differences, with some environmental variation. In any case, these fractional errors propagate directly into our measured dish power patterns.

## 4. DISH MEASUREMENTS

### 4.1. Power pattern measurements

feed misalignment vs surface imperfections (different across different feed heights) risk of cross-coupling tie-downs

We make dish power pattern measurements at 137 MHz as described in Sec. 3.1 with the feed at 4.5 m, 5.0 m, and 5.3 m height above the dish surface (see Fig. 1). In each configuration we collect data for 2–4 days, obtaining roughly 200 satellite passes. We exclude times when the received power is within 20 dB of the background level determined between passes, and then grid measured beam values into  $1.8^\circ$  HEALPix cells on the sky, rejecting outliers in the top or bottom 5% in each cell as a final guard against rare satellite identification problems or ADC saturation issues.

Fig. 6 shows the measured power patterns for these three feed heights for the EW (left panel) and the NS (right panel) feed polarizations. These maps are plotted in sine-projection with dashed circles marking zenith angles of  $20^\circ$ ,  $40^\circ$ ,  $60^\circ$ , and  $80^\circ$ . The sky coverage in these dish measurements extends out to typically  $\theta \sim 60^\circ$ , beyond which the ORBCOMM flux is sufficiently attenuated relative to diffuse galactic emission that power measurements are no longer clean probes of the antenna gains in the direction of the satellite. At these largest measurable zenith angles the beam sidelobes are roughly -30 dB and trending downward.

The roughly  $10^\circ$  main lobe narrows slightly as the feed is raised from 4.5 m to 5.3 m, and the sidelobes shrink both in size and in amplitude, confirming that the focus is closer to 5.3 m. As the response of the dish itself is azimuthally symmetric, its response with the feed should have the  $180^\circ$  symmetry of the dipole. Indeed, the observed main lobes of the EW (NS) beams are slightly wider in the NS (EW), especially in the 5.3 m feed height beam as it is most in focus. Unsurprisingly, we observe deviations from this symmetry in the sidelobes, which are very sensitive to slight dish/feed imperfections.

Figure 7 shows slices through the E and H planes of these power patterns along with the HFSS and CST numerical models discussed earlier. As in the previous plot, the EW and NS beams are shown in the left and right panels, while the different feed heights are shown in the different rows. The data agree with both models to within 1 dB in the main lobe, though often appear slightly shifted so they are not quite centered on zenith. The data diverge further in the sidelobes at zenith angles of  $20^\circ$  and larger. Here the evolution of the sidelobes as the feed is raised is again seen starkly, as is the fact that the main lobes are slightly wider along the H planes than along the E planes. We observe that both models agree with the measured beams in the main lobe but deviate differently at the 1–5 dB level in the sidelobes.

We emphasize that the model deviations observed in the measured beams are real in that they are larger than the 0.5 dB systematics observed in the null experiments (Fig. 5). Those experiments bound the impact of environmental reflections and reference dipole mismodeling to the max 10% level or smaller across the whole sky. The observed dish beam asymmetries, model deviations in sidelobes, and slight shifts of the main lobes all suggest feed centering errors. The feed is suspended by rope from three telephone poles spaced around the dish, and

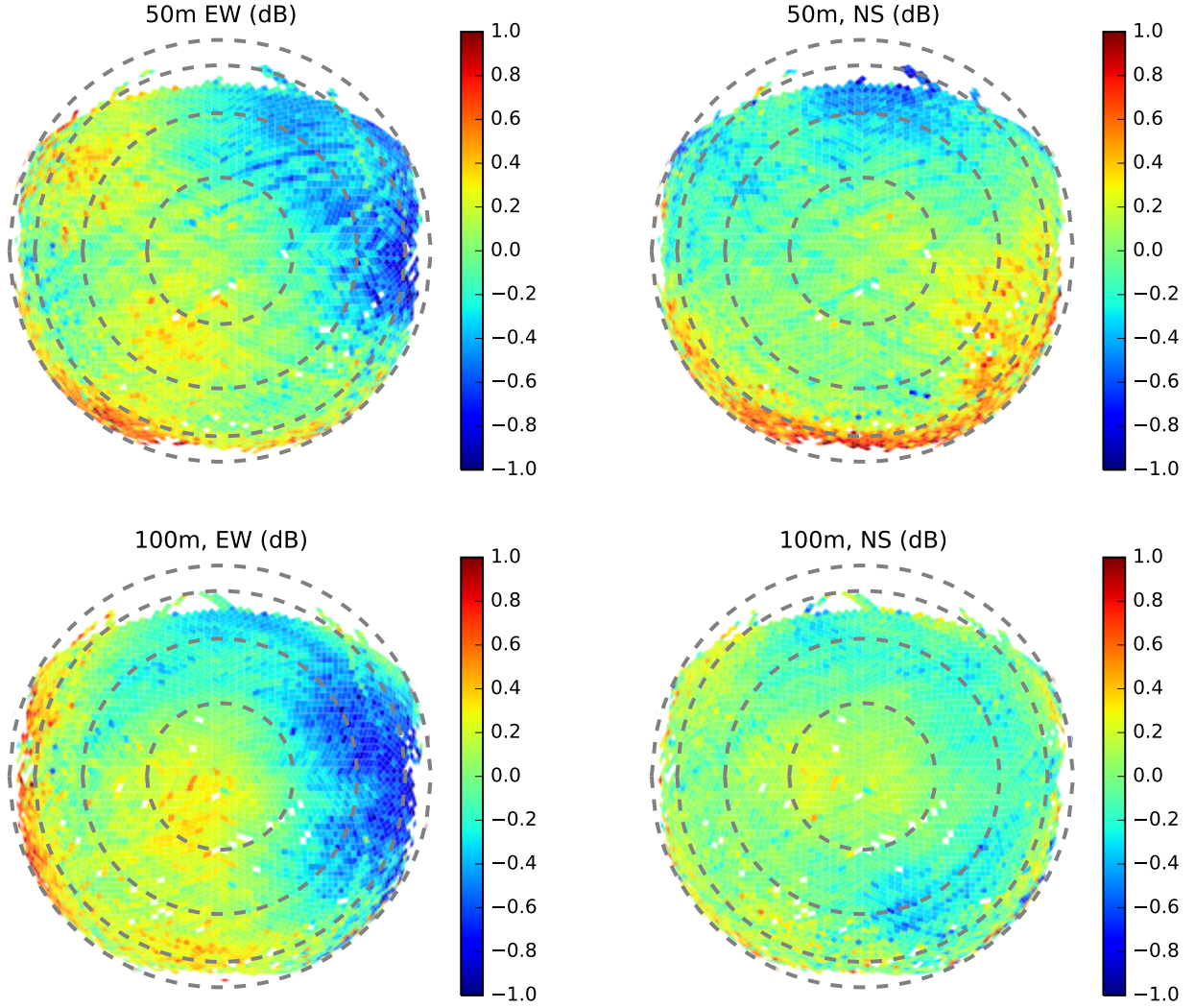


FIG. 5.— We characterize the accuracy of the beam measurement system through null experiments in which a second reference antenna is taken as the AUT and ratio of both reference antenna power patterns is measured for EW (left) and NS (right) polarizations. The reference antennas are separated by 50 m from each other and from the HERA dish in the first experiment (top), and by 100 m from each other and from the HERA dish in the second experiment (bottom).

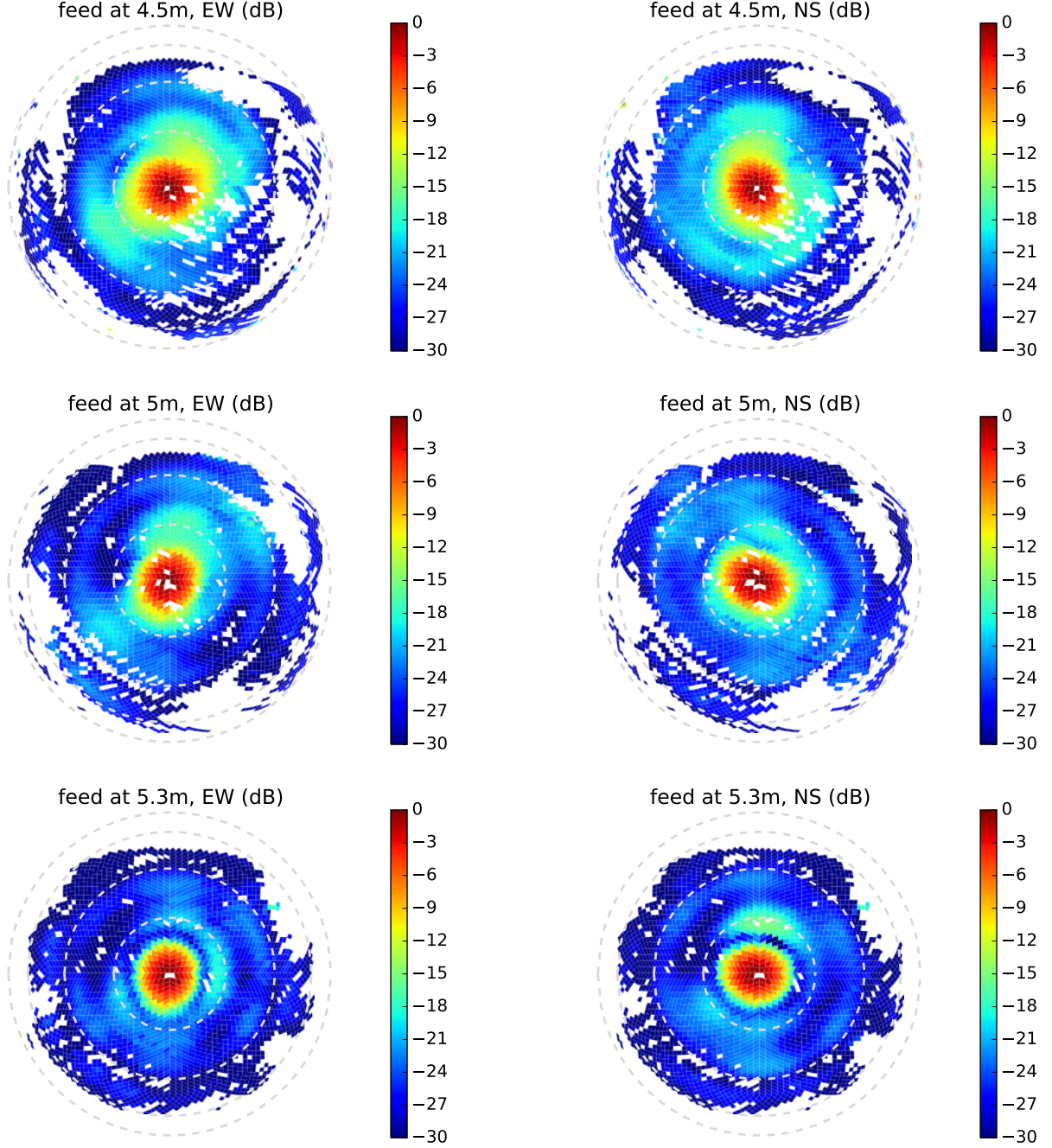


FIG. 6.— Measured dish power patterns with three feed heights for the EW (left panel) and NS (right panel) linear instrumental polarizations. The sidelobes shrink and the main lobe narrows as the feed is raised, confirming that the best focus of the dish/feed system is close to  $h_{\text{feed}} = 5.3$  m.

is raised by pulling all three ropes to a new length. Each time this is done the feed centering is slightly disturbed because all three ropes must be pulled to the exact same length to center the feed. If feed tilt/rotation errors or dish surface imperfections were significant, then the beam errors at different feed heights would look similar because these errors persist when the feed is raised or lowered. The fact that they change over the three beam measurements suggests that feed centering errors are most significant because they change when the feed height is changed. To mitigate these errors, the feeds in the full HERA array will be tied down to the dish

surface.

#### 4.2. Sensitivity

We compute the effective collecting areas of these beam patterns by first interpolating over unmeasured cells and smoothly extrapolating the power pattern to the horizon. These operations produce a realistically smooth beam which reaches roughly -30 dB at the horizon, as suggested by the numerical models. The collecting area  $A$  is related to the beam power pattern  $B(\theta, \phi)$  as

$$A = \frac{\lambda^2 B(0, 0)}{\int B(\theta, \phi) d\Omega} \quad (1)$$



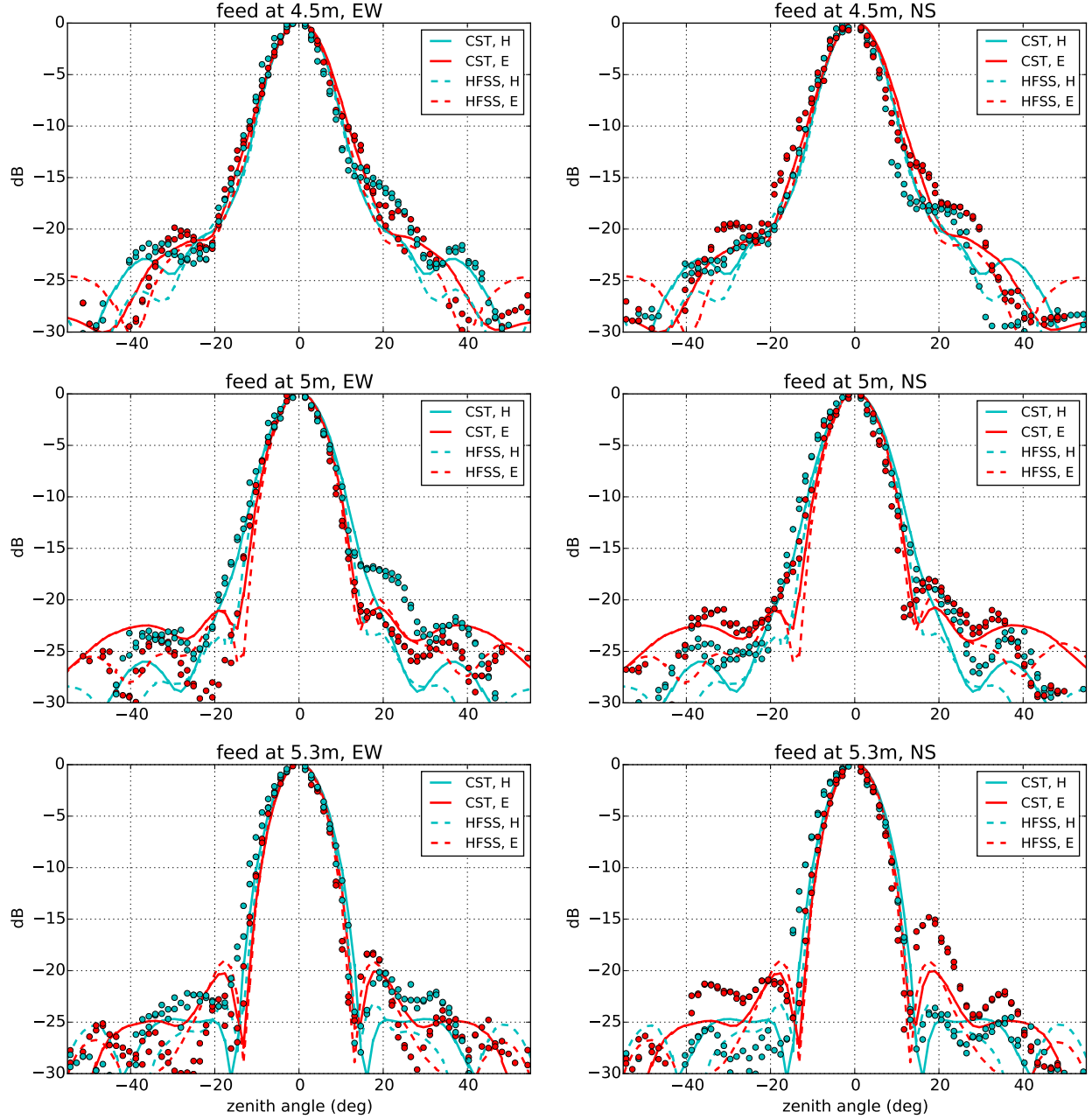


FIG. 7.— Slices through the E and H planes through the measured dish power patterns (points) and numerical models (curves). The measured beams agree with both models in the main lobe out to zenith angles of 15–20°, but begin to deviate in the sidelobes where the beam response is 25–30 dB down from zenith.

The collecting areas are shown in Table 1 along with the maximal collecting area achieved by the Airy pattern for a 14 m dish. The measured collecting areas are 30–50% lower than the geometric area. This is in line with expectations given that the Airy pattern has the largest possible collecting area, equal to the dish cross section, and the feed’s backplane and cylindrical skirt reduce it. However we opt for this reduction over added collecting area in order to reduce the azimuthal beam asymmetry and minimize the cross-coupling between adjacent dishes.

We run 21cmSense<sup>5</sup> to compute the overall SNR of a power spectrum detection with one season (6 hours

TABLE 1  
COLLECTING AREA (m<sup>2</sup>) OF MEASURED 137 MHz BEAMS AND CORRESPONDING POWER SPECTRUM SNR FOR HERA-331 USING EITHER FOREGROUND AVOIDANCE OR FOREGROUND SUBTRACTION.

Beam	$A_{\text{eff}}$ (m <sup>2</sup> )	SNR (avoidance, subtraction)
Airy pattern	155	25.5, 90.8
Measured, feed at 5.3 m	93.0	19.3, 74.3
Measured, feed at 5 m	77.1	16.4, 67.9
Measured, feed at 4.5 m	68.5	15.4, 63.9

per night for 180 nights) of HERA-331 data. We use a fiducial Epoch of Reionization model generated with 21cmFast (Mesinger et al. 2011). This model assumes  $\zeta = 31.5$  for the ionizing efficiency,  $T_{\text{vir}} = 1.5 \times 10^4$  K

<sup>5</sup> <https://github.com/jpober/21cmSense>



for the minimum virial temperature of halos producing ionizing photons, and  $R_{\text{mfp}} = 30 \text{ Mpc}$  for the mean free path of ionizing photons, and reaches 50% ionization at  $z \sim 9.5$  and complete ionization at  $z \sim 7$ , and is consistent with most current observations (e.g. Pober et al. 2014). We predict SNRs first for a foreground *avoidance* approach where only modes outside of the wedge plus a buffer of  $\Delta k_{\parallel} = 0.1 \text{ h Mpc}^{-1}$  are used. These modes have frequency dependence larger than that of any source on the sky. We also predict SNRs for a foreground *subtraction* approach using all modes whose instrumental frequency dependence is larger than that of a source at the edge of the main lobe.

The SNRs computed with the measured collecting areas are 15-20 with foreground avoidance compared with 25 for the Airy pattern. With foreground subtraction, the SNR falls from 90 with the Airy pattern to 60-75 with the measured collecting areas. In all cases this reduction is a loss of sensitivity, but a power spectrum detection is still always very significant at the  $15\sigma$  level or better.

### 5. FOREGROUND DELAY SPECTRUM SIMULATIONS

We consider now the effects of the beam power pattern on the apparent frequency dependence of the foregrounds. Thyagarajan et al., (submitted) discuss the apparent frequency dependence of foregrounds in more detail as well as methods to mitigate it such as delay space CLEANing. We focus in this section on the uncertainties in these foreground power spectrum simulations due to beam modeling uncertainties, but first discuss these foreground simulations themselves and their dependence on observing conditions.

We simulate foreground power spectra using different primary beam models at various local sidereal times (LSTs). We use frequency-independent model beams (evaluated at 137 MHz) to isolate the interferometric foreground frequency dependence. The added frequency dependence of the changing overall gain and beam shape versus frequency is addressed by the other papers in this series. Given that our measured dish power patterns agree well with both numerical models (HFSS and CST) in the main lobe but deviate in the sidelobes, and that these models make somewhat different assumptions about the dish surface, we take them as a representative pair of possible dish models. We use a feed height of 5 m, a compromise between collecting area and risk of coupling to adjacent dishes. We also include the Airy pattern for comparison as in Thyagarajan et al. (2015a). Beam models with weaker response near the horizon (such as the Airy pattern) downweight sources in this direction of high apparent frequency dependence. This reduces the magnitude of emission near the edge of the EOR window, reducing the risk it leaks inside. We use the per-baseline approach of Parsons et al. (2012a,b), simulating visibilities measured by specific baselines as a function of frequency, then computing the Fourier transform over frequency (delay transform) and normalizing the result into a cosmological power spectrum following Thyagarajan et al. (2015a).

In detail, we simulate visibilities for each beam model at various LSTs, modeling the sky as the sum of the Global Sky Model (de Oliveira-Costa et al. 2008) and the Culgoora (Slee 1995) and MWA Commissioning Sur-

vey (Hurley-Walker et al. 2014) point source catalogs, all evaluated at 150 MHz. We use a frequency spacing of 1 MHz, sufficient to characterize delays within and just outside of the horizon limits on both baseline lengths we are concerned with, 14.6 m and 43.8 m. We use a total bandwidth of 100 MHz (50 MHz after applying the Blackman-Harris window) centered on 150 MHz. This bandwidth is larger than the 10 MHz thought to be safe from signal evolution over redshift, but is the bandwidth used in the wide band delay space foreground filter of Parsons et al. (2014); Ali et al. (2015a).

Figure 8 (top panel) shows simulated foreground delay spectra at various LSTs using the nominal HFSS beam. As all these LSTs are high galactic latitudes far from the galactic center, the total visibility power (the level of the zero delay mode) varies only by a factor of a few over these LSTs on both baseline lengths (14.6 m (left panel), 43.8 m (right panel)). However the positive delay horizon limit (corresponding to the western horizon) has a peak that varies by over 1.5 orders of magnitude on both baseline, demonstrating the stark difference in horizon brightening when the galaxy is just above versus just below the horizon.

In this figure we perform the approximate conversion from delay  $\tau$  to  $k_{\parallel}$  at  $z = 8$ , which we plot as a second  $x$ -axis at the top of the plot. For these short baselines it is a good approximation to interpret  $k_{\parallel}$  as  $k$ , and we thus plot a 1D model power spectrum computed using 21cmFast (Mesinger et al. 2011) as a dotted line for comparison. Ftop panel

To characterize the effect of beam modeling uncertainties on this horizon brightening, we select two of these LSTs, one with maximal horizon brightening ( $2^\circ$ ), and one with minimal horizon brightening ( $62^\circ$ ). Figure 9 shows the sine-projected Global Sky Model at 150 MHz, which dominates the horizon brightening effect, in local Azimuth/Elevation coordinates with units of Kelvin for both LSTs. Dashed lines mark zenith angles  $20^\circ$ ,  $40^\circ$ ,  $60^\circ$ , and  $80^\circ$ . These plots confirm that the large negative delay peak at the  $0^\circ$  LST is due to the center of the galaxy just above the horizon. In contrast, several hours later, the galactic center is fully below the western horizon, leaving only a slight brightening near the eastern horizon due to the weaker galactic anticenter.

How much do the predicted foreground power spectra differ between the three model dish power patterns? Figure 8 (middle panel) shows the simulated delay spectra for all three beams at  $0^\circ$  LST, when the horizon brightening is worst. Both numerical models agree out to delays of roughly 20 ns on the 14.6 m baseline and 50 ns on the 43.8 m baseline. These numbers suggest that the beams track each other fairly well out to  $25^\circ$  from zenith, beyond which they diverge. This is roughly what is observed in Figure 7 (middle panel). At larger delays, especially near the positive delay horizon limit, all three model delay spectra diverge due to the significant edge brightening which effectively discriminates between these models. The CST, HFSS, and Airy beams reach roughly -35 dB, -38 dB, and -50 dB at the horizon (Figure 3), consistent with the fact that the CST beam has the largest horizon brightening, followed by the HFSS beam, and then by the Airy beam. This is seen in the delay spectra for both baseline lengths, though the edge brightening is much clearer on the longer baseline where it less diluted

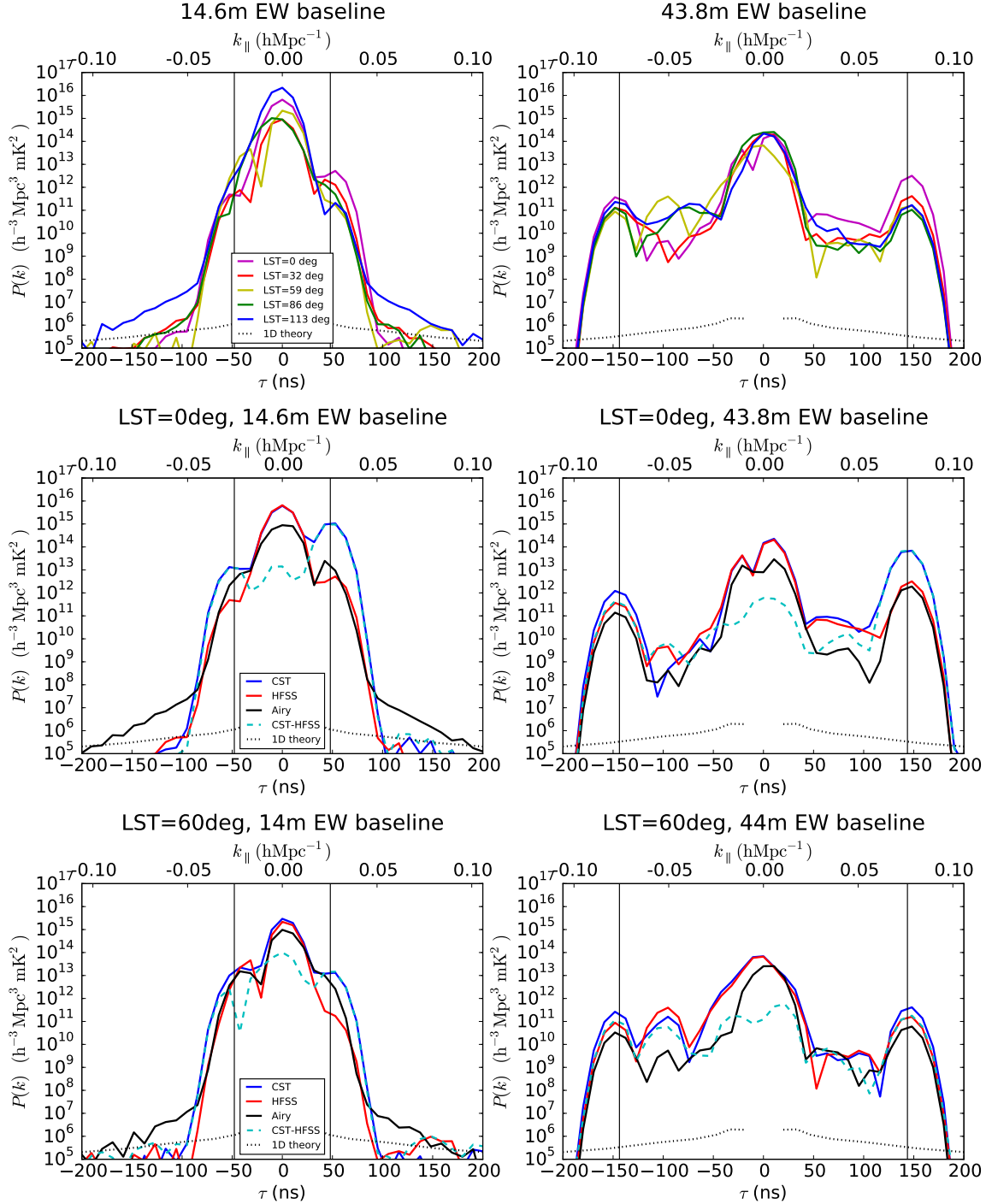


FIG. 8.— Simulated foreground delay spectra using the HFSS beam at various LSTs (top panel). We then plot the delay spectra at two LSTs spanning the range of possible horizon brightening for three different beam models. The maximum horizon brightening at the positive horizon occurs close to  $0^\circ$  LST (middle panel), and the three beam models thus differ markedly in their predicted delay spectra near the horizon. The horizon is shown in all panels as a vertical line at the baseline's maximum delay seen by radiation from the horizon in line with the baseline. In contrast, when the horizon brightening effect is smaller at  $60^\circ$  LST, the foreground delay spectra from all three beams agree.

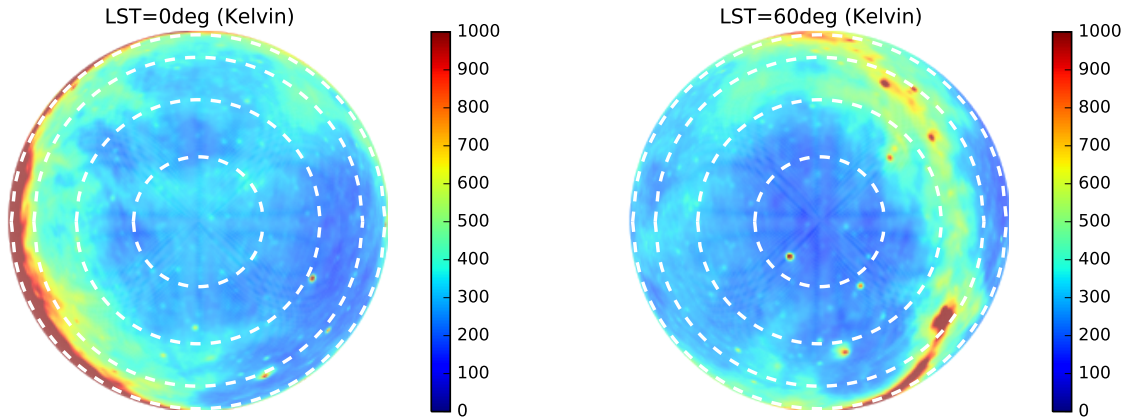


FIG. 9.— Global Sky Model (de Oliveira-Costa et al. 2008) in sine-projected horizontal coordinates at LST of  $2^\circ$  (left) and  $62^\circ$  right. The very bright emission from the center of the galaxy at the western horizon at  $2^\circ$  is seen in the delay spectra of EW baselines as a horizon brightening at negative delay.

by zero delay emission.

In contrast, all three models agree much more closely when there is little or no edge brightening as in Figure 7 (bottom panel) where we plot the delay spectra for all three beams for  $60^\circ$  LST. There is still a modest flattening off near the horizon on the 14.6 m baseline and a slight peak on the 43.8 m baseline due to the large solid angle near the horizon. However as the near horizon emission at this LST is roughly the same temperature as emission from everywhere else on the sky, the difference between the three beam models is greatly reduced.

## 6. DISCUSSION

Power spectrum analyses by first generation 21 cm observatories are ongoing, but are contending with challenges ranging from calibration and foreground modeling to the analysis effort required to process thousands of hours of data. HERA draws on the most successful ideas from these first generation instruments, pursuing a compact and redundant array layout and large collecting area antenna elements. The hexagonal grid allows redundant calibration and coherent power spectrum integration, and the large 14 m dish achieves sufficient sensitivity at a reasonable data processing and analysis cost. The papers in this series characterize the 14 m diameter dish used as HERA’s antenna element using reflectometry measurements and simulations which probe its frequency response, as well as power pattern measurement which probe its angular response.

We present in this paper beam pattern measurements at 137 MHz and discuss their implications for 21 cm power spectrum analysis in terms of sensitivity and foreground isolation. We begin with the power pattern measurements using the beam mapping system of Neben et al. (2015) which we deploy at the prototype three-element HERA array at the National Radio Astronomy Observatory–Green Bank. We present measured power patterns for three dish configurations with the feed at different heights over the dish surface in order to characterize the focus of the system. The measured power patterns probe nearly two thirds of the visible sky, down to  $-30$  dB relative to the zenith response. The measured beams agree well with both models in the main lobe out to  $10$ – $20^\circ$  from zenith, then roughly track the typical sidelobe levels at  $20$ – $30$  dB below zenith, deviating at the

1–5 dB level.

These deviations away from models and away from  $180^\circ$  azimuthal symmetry are larger than the  $\pm 1$  dB systematics observed in the null experiments which probe our beam measurement accuracy, suggesting they are genuine measurements of the in situ dish beam. The most likely dish non-idealities are dish surface imperfections and feed misalignment, both of which may vary from antenna to antenna in the full HERA array. Characterizing this antenna-to-antenna beam variation and its effects on power spectrum analyses for HERA, as Neben et al. (submitted) do for the MWA, is left as future work.

We quantify HERA’s 21 cm power spectrum sensitivity given our beam measurements by first computing the collecting area of the different dish configurations. We observe a reduction of 30–50% from the geometric cross section of a 14 m dish due to the dipole feed and its cylindrical skirt which tapers the beam towards the edge of the dish to mitigate cross coupling with adjacent dishes. We convert these collecting areas into effective dish sizes, then use 21cmSense to predict the overall power spectrum SNR with one season of HERA-331 data. We find SNRs of 18.7, 19.3, and 74.3 in the pessimistic, moderate, and optimistic foreground scenarios with the feed at optimal focus. While a reduction from the theoretical limit of an unobstructed 14 m aperture, these sensitivities still permit a very significant detection of the 21 cm signal after a single observing season.

Beyond simple sensitivity considerations, though, the beam pattern affects science analyses by reweighting celestial emission in different regions of the sky, which are then imprinted with different frequency dependence by the interferometer. Longer baselines are proportionately more susceptible to this effect, giving rise to a “wedge” shaped region in 2D Fourier space. Thyagarajan et al. (2015a) has highlighted that the distribution of foregrounds *within* the wedge is important as well. If the beam response is sufficiently shallow at low elevations, there is a brightening of emission from near the horizon in line with the baseline due in part to the large solid angle at low elevations. This produces a characteristic “pitchfork” shape in the delay spectrum of a single baseline, with a zero delay peak due to bright near-zenith emission surrounded by tines at the negative and pos-



itive horizon limits due to emission from the two horizon directions in line with the baseline. These horizon peaks are *most* at risk of leaking foreground power into the EOR window given chromatic instrumental responses such as bandpass miscalibration, though techniques are being developed to suppress emission from near the horizon (Parsons et al. 2015).

We predict the magnitude of this effect for the HERA element as well as its dependence on beam modeling uncertainties. As expected, we find that the level of horizon brightening is largest when the galaxy is just above the horizon, and lowest when it is well below. When the pitchfork effect is large, its uncertainty is also large as seen in the deviation of the delay spectra with HFSS and CST beam models in these simulations. When the effect is small, the two beam models produce much more similar results, highlighting the delay spectrum as an exquisite probe of the difficult-to-measure beam response at very

low elevations.

As discussed by the other papers in this series (Ewall-Wice et al., in prep, Patra et al., in prep, Thyagarajan et al., in prep), the frequency dependence of both the beam’s angular response and its overall gain widen the delay kernel of a source, leaking power into the EOR window out to  $k_{\parallel} = 0.15\text{--}0.23\text{ h Mpc}^{-1}$ . This is well inside the wedge plus buffer assumed in the moderate and pessimistic cases considered above. The optimistic case requires calibrating out the instrument frequency response enough to begin to access cosmological modes within the wedge. This is much more challenging, but the sensitivity gains are enormous as those signal modes are thought to be the strongest. Even in the pessimistic case, though, assuming only previously demonstrated analysis techniques, we project a  $18\sigma$  detection of the EOR power spectrum which would provide begin to probe reionization models in detail and shed light on our cosmic dawn.

## REFERENCES

- Ali, Z. S., et al. 2015a, *ApJ*, 809, 61  
—, 2015b, *ArXiv e-prints*  
Asad, K. M. B., et al. 2015, *ArXiv e-prints*  
Bernardi, G., et al. 2013, *ApJ*, 771, 105  
Bowman, J. D., et al. 2013, *TrottObservingModes*, 30  
Datta, A., Bowman, J. D., & Carilli, C. L. 2010, *ApJ*, 724, 526  
de Oliveira-Costa, A., Tegmark, M., Gaensler, B. M., Jonas, J., Landecker, T. L., & Reich, P. 2008, *MNRAS*, 388, 247  
Dillon, J. S., et al. 2014, *Phys. Rev. D*, 89, 023002  
Furlanetto, S., Oh, S., & Briggs, F. 2006, *Physics Reports*, 433, 181  
Górski, K. M., Hivon, E., Banday, A. J., Wandelt, B. D., Hansen, F. K., Reinecke, M., & Bartelmann, M. 2005, *The Astrophysical Journal*, 622, 759  
Hurley-Walker, N., et al. 2014, *PASA*, 31, 45  
Jelić, V., Zaroubi, S., Labropoulos, P., Bernardi, G., de Bruyn, A. G., & Koopmans, L. V. E. 2010, *Monthly Notices of the Royal Astronomical Society*, 409, 1647  
Liu, A., Parsons, A. R., & Trott, C. M. 2014a, *Phys. Rev. D*, 90, 023018  
—, 2014b, *Phys. Rev. D*, 90, 023019  
Liu, A., Tegmark, M., Morrison, S., Lutmirski, A., & Zaldarriaga, M. 2010, *MNRAS*, 408, 1029  
Loeb, A., & Furlanetto, S. R. 2013, *The First Galaxies In The Universe* (Princeton University Press, Princeton, NJ)  
Mesinger, A., Furlanetto, S., & Cen, R. 2011, *MNRAS*, 411, 955  
Moore, D., et al. 2015, *ArXiv e-prints*  
Moore, D. F., Aguirre, J. E., Parsons, A. R., Jacobs, D. C., & Pober, J. C. 2013, *The Astrophysical Journal*, 769, 154  
Morales, M. F., Bowman, J. D., & Hewitt, J. N. 2006, *ApJ*, 648, 767  
Morales, M. F., Hazelton, B., Sullivan, I., & Beardsley, A. 2012, *ApJ*, 752, 137  
Morales, M. F., & Wyithe, J. S. B. 2010, *Annual Reviews of Astronomy and Astrophysics*, 48, 127  
Neben, A. R., et al. 2015, *Radio Science*, 50, 614  
Paciga, G., et al. 2011, *Monthly Notices of the Royal Astronomical Society*, 413, 1174  
Parsons, A., Pober, J., McQuinn, M., Jacobs, D., & Aguirre, J. 2012a, *ApJ*, 753, 81  
Parsons, A. R., Liu, A., Ali, Z. S., & Cheng, C. 2015, *ArXiv e-prints*  
Parsons, A. R., Pober, J. C., Aguirre, J. E., Carilli, C. L., Jacobs, D. C., & Moore, D. F. 2012b, *ApJ*, 756, 165  
Parsons, A. R., et al. 2014, *ApJ*, 788, 106  
Pober, J. C., et al. 2013, *ArXiv e-prints*  
Pober, J. C., et al. 2014, *The Astrophysical Journal*, 782, 66  
Pritchard, J. R., & Loeb, A. 2012, *Reports on Progress in Physics*, 75, 086901  
Slee, O. B. 1995, *Australian Journal of Physics*, 48, 143  
Thyagarajan, N., et al. 2013, *The Astrophysical Journal*, 776, 6  
—, 2015a, *ApJ*, 804, 14  
Thyagarajan, N., et al. 2015b, *ApJ*, 807, L28  
Tingay, S. J., et al. 2013, *Publications of the Astronomical Society of Australia*, 30  
Trott, C. M., Wayth, R. B., & Tingay, S. J. 2012, *ApJ*, 757, 101  
van Haarlem, M. P., et al. 2013, *A&A*, 556, A2  
Vedantham, H., Udaya Shankar, N., & Subrahmanyam, R. 2012, *ApJ*, 745, 176  
Zaroubi, S. 2013, in *Astrophysics and Space Science Library*, Vol. 396, *The First Galaxies*, ed. T. Wiklind, B. Mobasher, & V. Bromm (Springer Berlin Heidelberg), 45–101  
Zheng, H., et al. 2014, *Monthly Notices of the Royal Astronomical Society*, 445, 1084  
Zheng, H., et al. 2014, *MNRAS*, 445, 1084